Fe foils with single-crystal-like texture for hyperfine interaction studies: Anisotropy of the hyperfine field in Fe

G. Seewald, E. Zech, E. Hagn, and H.-J. Körner
Physik-Department, Technische Universität München, D-85748 Garching, Germany
(Received 9 December 2002; revised manuscript received 14 April 2003; published 3 July 2003)

1-μm-thin polycrystalline Fe foils with sharp biaxial texture were produced. The importance of various preparation parameters for the sharpness of the texture was investigated. The use of the foils for nuclear magnetic resonance on oriented nuclei and modulated adiabatic fast passage on oriented nuclei measurements of the magnetic and electric hyperfine interactions of impurities in Fe was demonstrated by measurements on ^{192}Ir, ^{191}Pt, ^{198}Au, and ^{199}Au. In particular, it was found that a strain-induced electric field gradient can arise from the cooling down of the foils on the Cu sample holder. This additional electric field gradient could be avoided by a thick Fe crystal between the foils and the sample holder. The magnetic hyperfine fields of Ir, Pt, and Au in Fe were shown to differ between the [100] and [110] orientations of the magnetization by $B_{\mathrm{HF}}^{[100]} - B_{\mathrm{HF}}^{[110]} = -0.073(8)$ T, $-0.003(6)$ T, and $-0.016(9)$ T, respectively.

DOI: 10.1103/PhysRevB.68.014402 PACS number(s): 76.60.Jx, 75.50.Bb, 76.60.Gv, 76.80.+y

I. INTRODUCTION

For a long time about 1-μm-thick, coldrolled, polycrystalline Fe or Ni foils were the standard samples for nuclear magnetic resonance on oriented nuclei (NMR-ON) experiments. Many nuclear magnetic moments of unstable isotopes and many impurity hyperfine fields were determined using those samples.[1,2] In contrast to single crystals, the polycrystalline foils are cheap, easy to produce, and allow the production of radioactive impurities by neutron activation or recoil implantation.

It is well known that in these foils the crystallographic axes are not randomly oriented, but are more or less aligned along certain directions. This texture depends sensitively on details of the coldrolling and annealing during the preparation of the foils. It is also known that a suitable choice of the preparation parameters can lead to an almost uniform alignment of the crystallographic axes. This effect has been used, for example, to produce (100) oriented Ni substrates for epitaxial film growth of high-T_c superconducters.[3]

For hyperfine interaction studies the polycrystalline nature and the texture of the samples is without significance as long as the hyperfine interaction is independent of the angle between the magnetization and the crystallographic axes. However, the electric field gradient (EFG), which is in cubic Fe and Ni a spin-orbit effect, was recently shown to depend strongly on this angle.[4] Moreover, due to the anisotropy of the orbital moment,[5] even the magnetic hyperfine field should depend on the direction of the magnetization, although this anisotropy is expected to be very small in cubic lattice symmetry.

The idea was, therefore, to produce 1-μm-thick polycrystalline Fe foils with a single-crystal-like alignment of the crystallographic axes to combine the uniform orientation of the crystallographic axes in single crystals with the thinness and the less elaborate sample preparation of coldrolled foils. In the following we will refer to such polycrystalline foils with very sharp texture shortly as single-crystalline foils as opposed to bulk single crystals and ordinary polycrystalline foils.

A field where these single-crystalline foils may be particularly useful is the dependence of the hyperfine field on the crystallographic orientation of the magnetization. Presumably due to its smallness, this anisotropy has not been observed before, to our knowledge. A realistic idea of the expected order of magnitude can be obtained from the anisotropy of the magnetic moment of Fe and Ni, which is of the order of 1×10^{-4}.[6]

In this context, single-crystalline foils offer the following advantages: The demagnetization field in bulk single crystals is in general different for different orientations of the magnetization, if the sample shape and/or the position of the probe nuclei within the sample are not perfectly symmetric. The estimation of this ''anisotropy'' of the demagnetization field represents a source of error, which is absent in the case of thin foils, where the demagnetization field is negligible. Moreover, the inhomogeneous broadening of the magnetic resonance is often smaller in polycrystalline foils than in bulk single crystals. This may be due to difficulties in the surface preparation of the single crystals or to the spread of the demagnetization field in nonellipsoidal samples. In any case, a small linewidth is decisive, since the quadrupole splittings in Fe and Ni are so small that they readily disappear within the inhomogeneous broadening of the resonance. However, they must be resolved for a precise determination of the magnetic resonance frequency.

A further feature of the hyperfine interaction in thin Fe foils emerged in the course of the experiments: Evidence was found that, in addition to the spin-orbit-induced EFG, a strain-induced EFG was generated by the different thermal constriction of the Fe foil and the Cu sample holder during the cooling down of the sample to very low temperatures. This complex of problems—the use of single-crystalline foils to determine the hyperfine interaction, the anisotropy of the hyperfine field, and the strain-induced EFG—was investigated via the magnetic and electric hyperfine interactions of ^{192}Ir, ^{191}Pt, ^{198}Au, and ^{199}Au impurities in these foils.

II. PREPARATION OF SINGLE-CRYSTALLINE FOILS

Dilute Fe alloys were prepared by melting Fe (purity $>99.999\%$) with the desired amount of the impurity element

 ©2003 The American Physical Society

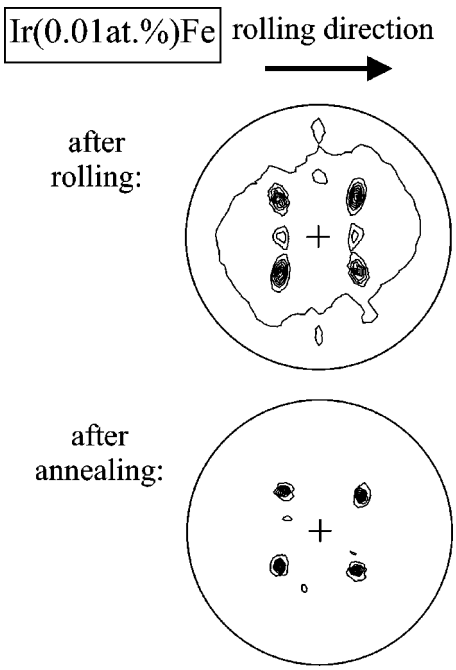

FIG. 1. Pole figure of the Fe (110) reflex of an Ir(0.01-at.%)Fe single-crystalline foil before and after the final annealing. The pattern with four peaks under 45° to the plane normal is characteristic for a (100) plane. The sharpness of the pattern is a direct measure of the sharpness of the texture.

in an electron beam furnace in high vacuum.

Single-crystalline foils with very sharp texture were produced in the following way: About 1-mm-thick pieces of the dilute alloy were sandwiched by 0.5-mm-thick stainless steel plates and rolled down to a thickness of about 1 μm. The thickness reduction per rolling pass was of the order of 5%. The rolling direction was held constant. After the rolling the foils were annealed for $\sim$4 h at $\sim$850 °C in high vacuum ($<10^{-7}$ mbar), and subsequently slowly (over $\sim$4 h) cooled down to room temperature. All experiments described below were performed on such foils.

The texture of the foils was characterized by pole figures.[7] Figure 1 shows the pole figures for an Ir(0.01 at. %)Fe alloy. The foil plane proved to be a (100) plane with the [110] directions in the plane parallel and perpendicular to the rolling direction. The orientation of the crystallographic axes was not perfectly uniform. The respective angular spread can be characterized by the full width of half-maximum $\Delta\beta$ across one of the peaks of the pole figure. For the example shown in Fig. 1, $\Delta\beta$ was about 6.5° after the annealing of the foil.

Figure 1 also illustrates the effect of the annealing: A distinct, but still rather irregular texture is already present before the annealing. Its distinctness is decisive for the sharpness of the texture after the annealing.

For the final sharpness of the texture, the following points proved to be important: (i) Heavy impurities, even in relatively small concentrations, promote the sharpness of the texture. This can be seen from Table I, where $\Delta\beta$ is listed for various alloys: $\Delta\beta$ is distinctly larger in pure Fe foils or foils with $3d$ impurities than in foils with $5d$ impurities. This

TABLE I. Angular spread (full width of half-maximum) of the texture of various dilute Fe alloys. The error of $\Delta\beta$ is of the order of 1°.

Alloy	$\Delta\beta$ (deg)	Alloy	$\Delta\beta$ (deg)
Au(0.01%)Fe	5.4	Ru(0.2%)Fe	8.0
Pt(0.1%)Fe	8.4	Ni(0.1%)Fe	9.6
Ir(0.01%)Fe	6.5	Co(1%)Fe	12.0
Os(0.1%)Fe	7.0	pure Fe	10.4

effect is also illustrated in Fig. 2, where the pole figures of a pure Fe foil are shown. (ii) The thickness of the samples had to be reduced during the rolling by at least a factor of 100 to obtain a sufficiently strong texture before the annealing. (iii) The foils should be annealed only after the final thickness is reached: The rolling of annealed foils distinctly reduced the already achieved sharpness of the texture. (iv) During the annealing the sharpness of the texture approaches a limit that depends on the texture before the annealing. The used temperature and duration of the annealing were well sufficient to reach this limit. Annealing for longer times or at higher temperatures led to no significant improvement of the texture.

No efforts were undertaken to increase the grain size, for example, by prolonged annealing, since for hyperfine interaction studies only the uniform orientation of the crystallographic axes is decisive.

Several attempts to produce single-crystalline Ni foils in the same way failed. The produced Ni foils were clearly textured, but the texture had several different components and was not sharp. In this context the thickness of the foils seems to be important: Ni foils that were rolled down to

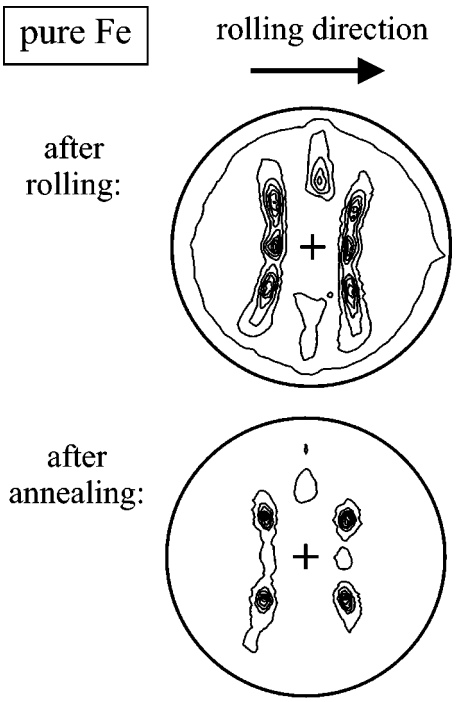

FIG. 2. (110) pole figure of a pure Fe single-crystalline foil before and after the final annealing.

10-μm thickness showed a moderately uniform texture after the annealing, and about 100-μm-thick Ni tapes with sharp texture are commercially available.

III. EXPERIMENTAL TECHNIQUES

The radioactive probe nuclei were produced by neutron irradiation of the single-crystalline Fe foils, either at the Munich FRM I reactor for 10 d by 7×10^{13} $n/(\mathrm{cm}^2\,\mathrm{s})$ or at the research reactor in Jülich for 26 d by 1.8×10^{14} $n/(\mathrm{cm}^2\,\mathrm{s})$. In the first case six 4×8 mm^2 pieces of the foils were used, in the latter case only one piece. After the irradiation the foils were annealed for 1 h at $\sim700\,^\circ$C to heal out the lattice damage due to the irradiation.

The impurity concentrations were 0.01-at.% Ir for the experiment on ^{192}Ir, 0.1-at.% Pt (^{190}Pt isotopically enriched to 5.7%) for the experiment on^{191}Pt, and 0.01-at.% Au and 0.1 at.% Pt (unenriched) for the experiment on ^{198}Au and^{199}Au. The respective spreads in the texture were about $\Delta\beta=6.5°$, 8.4°, and 7.4°.

The hyperfine interaction was measured by NMR-ON. This NMR technique uses as the signal the anisotropic emission of the γ radiation from oriented radioactive probe nuclei: The NMR-ON spectrum is the γ anisotropy recorded as a function of the applied rf frequency.[1] Due to the radiative detection of the resonance, NMR-ON is very sensitive and, therefore, well suited to investigate the hyperfine interaction at impurity atoms and the nuclear moments of unstable isotopes.

To orient the nuclei, the foils were soft soldered with GaIn to a Cu sample holder, mounted into a ^{3}He-^{4}He-dilution refrigerator, and cooled down to about 10 mK. The temperature was measured by a separate ^{60}CoCo(hcp) nuclear orientation thermometer on the sample holder. A magnetic field of up to 1.7 T could be applied by a superconducting magnet. Four Ge detectors were placed at 0°, 90°, 180°, and 270° with respect to the magnetic field to measure the γ anisotropy. In most cases the count rate ratio

$$\epsilon=[W(0°)+W(180°)]/[W(90°)+W(270°)]-1 \quad (1)$$

was analyzed.

The sample was mounted in such a way that the magnetic field was applied either along one of the [100] directions within the foil plane ([100] geometry), or along one of the [110] directions within the foil plane ([110] geometry), or along the [100] direction perpendicular to the foil plane (90° geometry). The sample-plane normal pointed to the 90° detector in [100] and [110] geometries, and to the 0° detector in 90° geometry. These are the nominal orientations. Deviations arose from the angular spread of the crystallographic orientations around the rolling direction, which can be characterized by $\Delta\beta$, and from the unavoidable misalignment of the sample relative to the magnetic field, which was less than 3°.

In Fe the electric hyperfine interaction is much smaller than the magnetic hyperfine interaction. The NMR spectrum of an isotope with nuclear spin I consists of $2I$ equidistant subresonances. The resonance between the magnetic substates $|m\rangle$ and $|m+1\rangle$ is given by

$$\nu_{m,m+1}=\nu_m-\Delta\nu_Q(m+1/2). \quad (2)$$

The subresonance between the most populated sublevels $m=I$ and $m=(I-1)$ is referred to as the ν_1 resonance, the subresonance between $m=(I-1)$ and $m=(I-2)$ as the ν_2 resonance, and so on.

The magnetic resonance frequency ν_m and the subresonance separation $\Delta\nu_Q$ are related to the hyperfine field and the EFG by

$$\nu_m=\left|\frac{g\mu_N}{h}(B_{\mathrm{HF}}+KB_{\mathrm{ext}})\right|, \quad (3)$$

$$\Delta\nu_Q=\frac{eQV_{z'z'}}{h}\frac{3}{2I(2I-1)}. \quad (4)$$

Here g is the nuclear g factor, μ_N is the nuclear magneton, B_{HF} is the hyperfine field, B_{ext} is the external magnetic field, K is a parameter that describes Knight shift and diamagnetic shielding, eQ is the nuclear quadrupole moment, and $V_{z'z'}$ is the $z'z'$ component of the EFG tensor. z' denotes the direction of the magnetization.

If the subresonance structure of the resonance is clearly resolved, ν_m and $\Delta\nu_Q$ can be determined directly from the NMR-ON spectrum. If the inhomogeneous broadening of the resonance is larger than the quadrupole splitting, the quadrupole splitting can be determined by modulated adiabatic fast passage on oriented nuclei (MAPON).[8,9] This technique uses an adiabatic fast passage of two rf fields with fixed frequency separation $\Delta\nu$. The γ anisotropy after this ''modulated passage'' is recorded as a function of $\Delta\nu$. This MAPON spectrum is, apart from a prefactor, the integral over the distribution $P(\Delta\nu_Q)$ of the quadrupole splitting. For more details to the MAPON technique we refer to Refs. 8–10.

The dependence of $V_{z'z'}$ on the direction of the magnetization allows to separate different contributions to the EFG. The spin-orbit-induced part of $V_{z'z'}$ is in lowest-order perturbation theory of the following form[11]:

$$V_{z'z'}^{\mathrm{so}(0)}+V_{z'z'}^{\mathrm{so}(2)}(\alpha_x^2\alpha_y^2+\alpha_y^2\alpha_z^2+\alpha_z^2\alpha_x^2). \quad (5)$$

α_x, α_y, and α_z are the directional cosines between the direction of the magnetization and the cubic axes x, y, and z. If there is a lattice distortion with axial symmetry along the z axis, there is an additional contribution to $V_{z'z'}$ of the form

$$V_{zz}^{\mathrm{dis}}(3/2\alpha_z^2-1/2), \quad (6)$$

where V_{zz}^{dis} is the principal component of the respective EFG.

To analyze the anisotropy of $\Delta\nu_Q$ in this work, the following parametrization of $\Delta\nu_Q$ proved to be convenient: The spin-orbit-induced part of $\Delta\nu_Q$ was described by its values for [100] and [110] orientation of the magnetization, $\Delta\nu_Q^{[100]}$ and $\Delta\nu_Q^{[110]}$. The lattice-distortion-induced part of $\Delta\nu_Q$ was described by its value for z orientation of the magnetization, $\Delta\nu_Q^{\mathrm{dis}}$. The z axis of the lattice distortion was assumed to be perpendicular to the plane of the sample foil. In [100] and

[110] geometry the magnetization remains within the (100) plane of the foil (*xy* plane). Equations (5) and (6) then imply the following dependence of the quadrupole splitting on the angle θ between the magnetization and the [100] direction:

$$\Delta\nu_Q(\theta)=\Delta\nu_Q^{[100]}\cos^2(2\theta)+\Delta\nu_Q^{[110]}\sin^2(2\theta)-1/2\Delta\nu_Q^{\mathrm{dis}}. \tag{7}$$

In the 90° geometry the magnetization also remains within a (100) plane, but now the *xz* plane, which is perpendicular to the sample plane. The quadrupole splitting is then given as a function of the angle θ between the magnetization and the [100] direction within the sample plane by

$$\Delta\nu_Q(\theta)=\Delta\nu_Q^{[100]}\cos^2(2\theta)+\Delta\nu_Q^{[110]}\sin^2(2\theta)+\Delta\nu_Q^{\mathrm{dis}}[3/2\sin^2(\theta)-1/2]. \tag{8}$$

IV. EXPERIMENTAL RESULTS

A. ^{192}IrFe

In a first experiment [experiment I(c)], the single-crystalline foils were soldered directly onto the sample holder and measurements were performed in [100] and [110] geometries. In a second experiment [experiment II(c)], these measurements were repeated on a newly prepared set of foils and additional measurements were performed in a 90° geometry. Finally [experiment II(i)], one of the foils was soldered on a thick Fe crystal which was in turn soldered on the sample holder. In this configuration measurements were performed in [100] and [110] geometries.

This set of measurements became necessary for the following reason: In the experiment I(c), $\Delta\nu_Q^{[110]}/\Delta\nu_Q^{[100]}=0.724(14)$ was observed, whereas $\Delta\nu_Q^{[110]}/\Delta\nu_Q^{[100]}=0.643(8)$ was known from experiments on ^{188}Ir and ^{189}Ir in Fe single crystals.[4] To explain this discrepancy by a deviation of the actual from the nominal orientation of the magnetization—either due to an erroneous orientation of the foils or due to the presence of texture components that are not visible in the pole figures—the deviation would had to be of the order of 10° in each geometry. This was rather improbable.

Therefore, the following hypothesis was developed: The cooling down of the Fe foils on the Cu sample holder leads, due to the different thermal expansion coefficients of Fe and Cu, to a lattice distortion with symmetry axis perpendicular to the foil plane, which in turn induces an EFG with principal axis perpendicular to the plane. For IrFe the respective strain-induced contribution to the quadrupole splitting has the same sign as the spin-orbit-induced quadrupole splitting and brings the ratio $\Delta\nu_Q^{[110]}/\Delta\nu_Q^{[100]}$ closer to 1. For some reason this effect is much smaller for bulk Fe crystals.

The additional measurements tested this hypothesis in two ways: First, if the discrepancy between the quadrupole splittings in foils and bulk single crystals is due to the thermal constriction of the sample holder, it should be removed by the Fe crystal between the foils and the sample holder. Second, if an additional EFG with symmetry axis perpendicular to the foil plane is present, its contribution to the quadrupole splitting should change the sign and become twice as large when the sample is magnetized perpendicular to its plane in the 90° geometry.

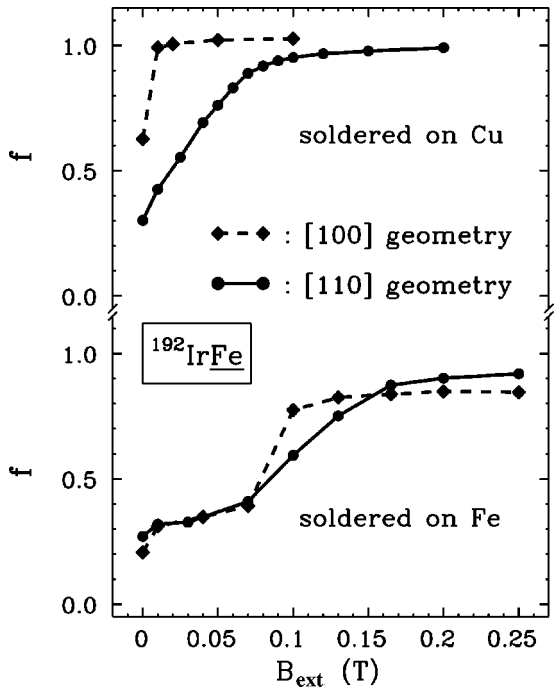

FIG. 3. ^{192}IrFe: Magnetization curves in [100] and [110] geometries without (top) and with (bottom) thick Fe crystal between foil and Cu sample holder. The γ anisotropy of the 468 keV transition was analyzed.

The Fe single-crystal disk between the foil and the sample holder in the experiment II(i) was 0.51 mm thick and 10 mm in diameter. Its plane was a (100) plane as the plane of the foil, and its crystallographic axes within the plane were also always oriented in the same way as those of the foil. Only one 4×4-mm^2 foil was placed in the center of the single-crystal disk to minimize the asymmetry in the demagnetization field.

In the 90° geometry a special sample holder was used that faced the magnetic field instead of being parallel to it. In addition, a special ^{60}CoCo(hcp) nuclear orientation thermometer was used with *c* axis perpendicular to the thermometer plane to ensure that the magnetic field and the magnetization of the thermometer are always parallel.

1. γ anisotropy measurements

The orientation of the magnetization by the magnetic field was monitored via the respective increase of the γ anisotropy. Figure 3 shows the respective magnetization curves for [100] and [110] geometries. The quantity *f* in Fig. 3 is the attenuation of the γ anisotropy ϵ with respect to the expected value for complete orientation of the magnetization.

The orientation along the magnetic field saturated at almost zero field in [100] geometry and at about 0.06 T in the [110] geometry, in accordance with the magnetic anisotropy energy of Fe. If the thick Fe crystal was used as the substrate, the saturation was shifted towards higher fields, in accordance with a demagnetization field of about 0.1 T. All

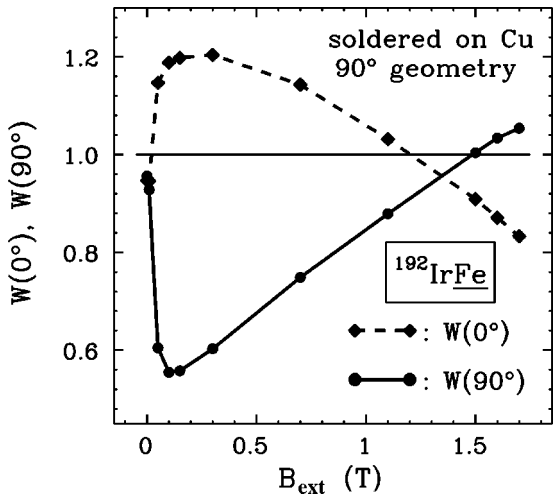

FIG. 4. ^{192}IrFe, 90° geometry: Count rates (468 keV transition) in the 0° and 90° detectors as a function of the magnetic field. The rates are normalized to 1 for isotropic γ emission. The temperature varied only slightly between 11.7 and 13.7 mK.

NMR-ON and MAPON measurements in [100] and [110] geometries were performed well above the respective saturation fields.

In 90° geometry a magnetic field of 2.2 T is necessary to overcome the demagnetization field and orient the magnetization perpendicular to the foil plane. But the maximum available field was only 1.7 T. Therefore, the orientation was incomplete, and the direction of the magnetization had to be determined via the γ anisotropy.

Figure 4 shows the normalized count rates in the 0° and 90° detectors as a function of the magnetic field. To understand this magnetization curve, it is useful to recall that the magnetic field is applied perpendicular to the foil plane towards the 0° detector, and that for ^{192}Ir the γ emission parallel to the orientation axis is reduced by roughly twice the amount by which it is enhanced perpendicular to the orientation axis.

In zero field the γ anisotropy was very small, pointing to a rather random distribution of the orientation of the magnetization. The application of a small field led to a relatively complete in-plane orientation of the magnetization towards the 90° detector: About 75% of the γ anisotropy which is expected for this orientation were reached at 0.15 T. This was probably due to a small in-plane component of the magnetic field, which resulted from a slightly imperfect orientation of the sample holder, especially with respect to rotations within the detector plane.

With increasing field the magnetization was rotated out of the plane towards the 0° detector. Accordingly, in the magnetization curve the roles of the 90° and 0° detectors are successively interchanged. The relative size of the normalized count rates in the 0° and 90° detectors can be used to determine the direction of the magnetization. For example, the angle θ between the magnetization and the foil plane is 45°, if the count rates in both detectors are equal. This was the case at a field of about 1.35 T.

At 1.7 T, where the MAPON measurement in the 90° geometry was performed, the normalized count rates in 0° and 90° could be described by $\theta = 64(7)°$ and an attenuation factor $f = 0.47(9)$. The large attenuation makes the determination of θ somewhat ambiguous, since it shows that at least in part of the sample strongly different orientations of the magnetization were present. Nevertheless, $\theta = 64(7)°$ was used for the interpretation of the measured quadrupole splitting, assuming that most of the MAPON signal came from a fraction of probe nuclei with relatively uniform magnetization behavior, whereas the γ anisotropy from the rest of the sample largely canceled out. This assumption was supported by the amplitudes of the MAPON signal in the 0° and 90° detectors, which showed that the signal came from nuclei with $\theta > 55°$, and by the relatively small width of the MAPON spectrum, which precluded a large spread in the orientation of the relevant probe nuclei.

The rotation of the magnetization out of the sample plane proceeded distinctly faster than calculated. At 1.7 T, for example, $\theta = 50.4°$ is predicted, if the magnetic field is applied exactly perpendicular to the foil plane, and $\theta = 47.0°$ for a realistic misorientation of 2.5°. It is not clear why the perpendicular orientation was less disfavored than expected. The presence of the Co(hcp) thermometer at the other side of the sample holder, the formation of a favorable domain structure, or the lattice distortion along the sample normal may have played a role.

2. NMR-ON measurements

Figure 5 shows as an example the NMR-ON and MAPON spectra in the [100] geometry at $B_{ext} = 0.1$ T of the experiment I(c). The NMR-ON spectrum shows an only partially resolved subresonance structure. Its shape can be well described by the superposition of the first five subresonances, if the inhomogeneous broadening of the quadrupole splitting is taken into account, which broadens the ν_1 resonance much more than the ν_4 and ν_5 resonances.

Figure 5 also illustrates the importance of the MAPON technique: In principle the information on the quadrupole splitting is already contained in the NMR-ON spectrum. But its derivation can be problematic, if the spectrum shape is already rather involved. The direct determination of the quadrupole splitting by MAPON establishes the quadrupolar origin of the shape of the NMR-ON spectrum, and avoids the need to make assumptions on the distribution of ν_m.

The quadrupole splittings that were deduced from the NMR-ON and MAPON spectra were in some cases slightly different. For example, $\Delta\nu_Q = -1.132(6)$ MHz was deduced from the MAPON data of Fig. 5, whereas $\Delta\nu_Q = -1.186(12)$ MHz was deduced from the NMR-ON data. This may point to the presence of regions with slightly different quadrupole splittings that are differently weighted by the NMR-ON and MAPON techniques. Or the extraction of the quadrupole interaction from NMR-ON spectra with strongly overlapping subresonances is not as accurate as suggested by the results of the *least squares* fit.

Consequently, the MAPON result was regarded as the more reliable value and adopted as the final result for the quadrupole splitting. However, the NMR-ON spectrum was

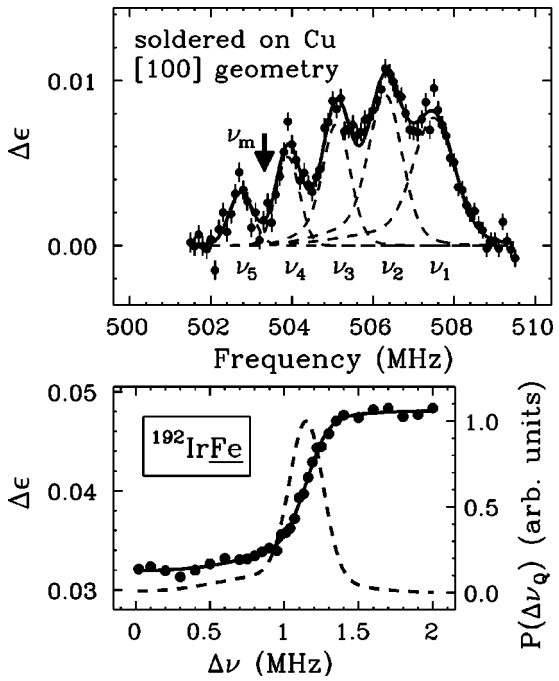

FIG. 5. ^{192}IrFe, experiment I(c), [100] geometry, $B_{\rm ext}=0.1$ T. Top: NMR-ON spectrum. Frequency modulation bandwidth $\Delta_{\rm FM}=\pm 0.15$ MHz, $T=42(5)$ mK. Bottom: MAPON spectrum. MAPON sweep from 510 to 496 MHz in 0.05 s. The dashed lines in the NMR-ON spectrum are the individual subresonances. The dashed line in the MAPON spectrum is its first derivative, which is proportional to $P(\Delta\nu_Q)$. The γ anisotropies of the 308-, 316-, and 468-keV transitions were combined to improve the statistics.

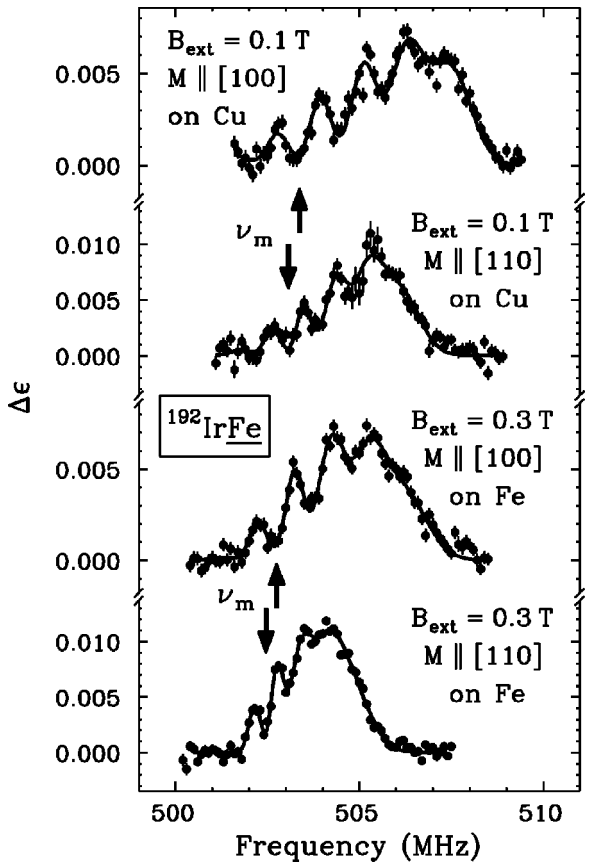

FIG. 6. ^{192}IrFe, experiments II(c) and II(i): NMR-ON spectra in [100] and [110] geometries. The arrows mark the position of ν_m.

interpreted with the quadrupole splitting as a free parameter, to ensure that the average quadrupole splitting as it is seen by the NMR-ON technique is used to determine ν_m.

Care was taken to optimize the amplitudes of the ν_4 and ν_5 resonances by an appropriate choice of the rf power and the temperature. In particular, the temperature was relatively high (between 40 and 70 mK) to ensure a sufficient population of the respective sublevels. Since ν_m is exactly in the middle between these subresonances, and since they are also the least broadened by the inhomogeneous broadening of the quadrupole splitting, they are especially important for a reliable determination of ν_m.

Figure 6 shows some of the NMR-ON spectra in [100] and [110] geometries, with and without a thick Fe crystal between the sample holder and the foil. It demonstrates that there is a very small but distinct difference in the magnetic hyperfine splitting between the [100] and [110] orientations of the magnetization. The measured ν_m's in [100] and [110] geometries are listed and compared in Table II. If all results are combined, the following anisotropy of ν_m is obtained:

$$\nu_m^{[100]}-\nu_m^{[110]}=+0.27(3)\ \ \text{MHz}.$$

3. MAPON measurements

Figure 7 shows some of the MAPON spectra in [100], [110], and 90° geometries, with and without a thick Fe crystal between the sample holder and the foil. It demonstrates that the hypothesis of an additional strain-induced EFG was essentially confirmed: (i) The distinct reduction of the quadrupole splittings by the thick Fe crystal is in line with the expected removal of the additional EFG. (ii) The smallest quadrupole splitting was observed in 90° geometry. This is in line with the expected sign change of the strain-induced part of the quadrupole splitting in this geometry.

We also note that the inhomogeneous broadening of the quadrupole splitting is larger in the [100] geometry than in the [110] geometry. This has also been observed in bulk single crystals.[4]

To obtain $\Delta\nu_Q$, a Gaussian distribution of the quadrupole splitting was assumed and the center of the distribution was fitted to the MAPON data. The results of all MAPON measurements are listed in Table III.

TABLE II. ^{192}IrFe: Magnetic resonance frequencies in [100] and [110] geometries.

Experiment	$B_{\rm ext}$ (T)	$\nu_m^{[100]}$ (MHz)	$\nu_m^{[110]}$ (MHz)	$\nu_m^{[100]}-\nu_m^{[110]}$ (MHz)
I(c)	0.1	503.327(23)	503.113(14)	0.214(27)
II(c)	0.1	503.373(27)	503.071(25)	0.302(37)
II(i)	0.2	503.113(37)	502.843(29)	0.270(47)
,,	0.3	502.755(19)	502.465(11)	0.290(22)

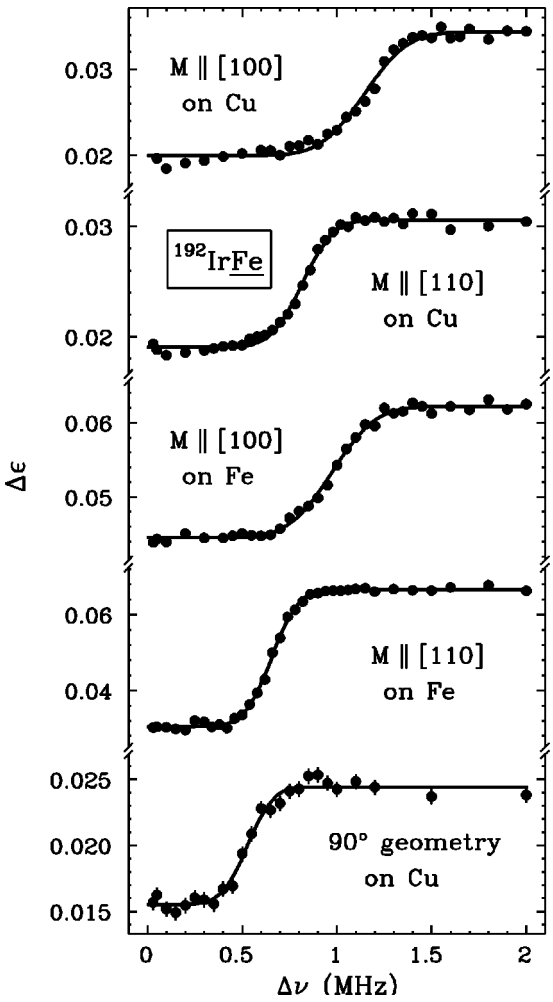

FIG. 7. ^{192}IrFe, experiments II(c) and II(i): MAPON spectra in [100], [110], and 90° geometries.

The reproducibility of the results was tested in several ways: The measurements of the experiment I(c) were repeated in the experiment II(c) on a new sample with essentially the same results. In the [110] geometry the quadrupole splitting was measured at two different magnetic fields. The agreement of the respective results confirmed that the magnetization was completely oriented. Only in the experiment I(c) in the [100] geometry slightly different quadrupole splittings were obtained at different magnetic fields. The most probable explanation are inhomogeneities in the strain-induced EFG that were correlated with inhomogeneities in the magnetic field dependence of the MAPON signal.

TABLE III. ^{192}IrFe: Quadrupole splittings in [100], [110], and 90° geometries.

Experiment	Geometry	B_{ext} (T)	$\Delta\nu_Q$ (MHz)
I(c)	[100]	0.005	−1.102(8)
”	”	0.1	−1.132(6)
”	”	0.3	−1.185(8)
II(c)	”	0.01	−1.143(12)
II(i)	”	0.2	−0.976(7)
I(c)	[110]	0.1	−0.824(5)
”	”	0.2	−0.831(9)
II(c)	”	0.1	−0.824(6)
”	”	0.15	−0.817(6)
II(i)	”	0.2	−0.656(3)
”	”	0.3	−0.666(4)
II(c)	90°	0.1	−1.108(11)
”	”	1.7	−0.529(11)

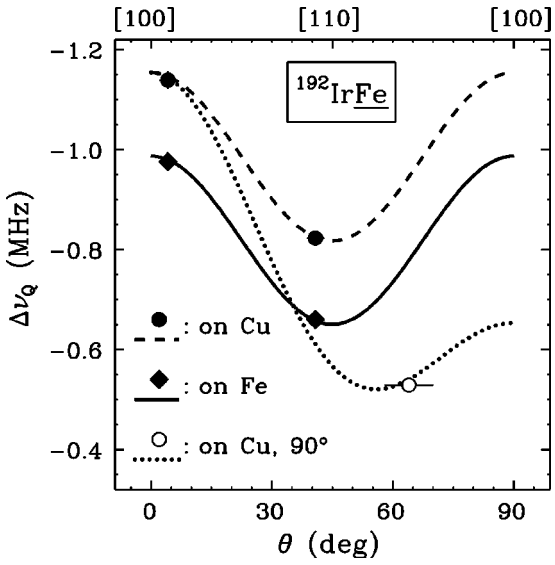

FIG. 8. ^{192}IrFe: Quadrupole splitting as a function of the angle between the magnetization and the [100] direction within the foil plane. Solid line: $V_{zz}^{dis}=0$. Dashed line: $V_{zz}^{dis}\neq 0$, magnetization within the foil plane. Dotted line: $V_{zz}^{dis}\neq 0$, magnetization within one of the other (100) planes. The data points are the observed quadrupole splittings.

Equations (7) and (8) were used for the quantitative interpretation of the observed quadrupole splittings. To take the scatter of the crystallographic orientation and a possible misalignment of the foils into account, $\theta=4.2(2.1)°$ was assumed in the [100] geometry and $\theta=40.8(2.1)°$ in the [110] geometry. In the 90° geometry at $B_{ext}=1.7$ T, $\theta=64(7)°$ was assumed. The three parameters $\Delta\nu_Q^{[100]}$, $\Delta\nu_Q^{[110]}/\Delta\nu_Q^{[100]}$, and $\Delta\nu_Q^{dis}$ were determined via *least squares* fit with the following results:

$$\Delta\nu_Q^{[100]}=-0.987(14)\ \text{MHz},$$

$$\Delta\nu_Q^{[110]}/\Delta\nu_Q^{[100]}=0.659(15),$$

$$\Delta\nu_Q^{dis}=+0.334(16)\ \text{MHz}.$$

$\Delta\nu_Q^{[110]}/\Delta\nu_Q^{[100]}$ is in agreement with 0.643(8), known from experiments on single-crystal samples.[4] This shows that the Fe crystal between the sample holder and the foil completely removed the discrepancy in the EFG between single-crystalline foils and bulk single crystals.

Figure 8 illustrates this interpretation of the observed quadrupole splittings: The anisotropy of $\Delta\nu_Q$ in the (100) plane is shown without V_{zz}^{dis} (solid line), when the foils are

soldered on a thick Fe backing, and with V_{zz}^{dis}, when the foils are directly soldered on the Cu sample holder. In the latter case the quadrupole splitting is simply shifted by $-1/2\Delta\nu_Q^{\mathrm{dis}}$, if the magnetization remains in the *xy* plane ([100] and [110] geometries, dashed line). Or the shift in the quadrupole splitting changes from $-1/2\Delta\nu_Q^{\mathrm{dis}}$ to $\Delta\nu_Q^{\mathrm{dis}}$, if the magnetization rotates in the *xz* plane (90° geometry, dotted line). The lines are predicted by the parameter set quoted above. The good agreement with the observed $\Delta\nu_Q$'s demonstrates the consistency of this description.

It should be noted that $\Delta\nu_Q^{\mathrm{dis}}$ was determined in two independent ways: By the different quadrupole splittings with and without Fe crystal between the foil and the sample holder, and by the different quadrupole splittings for in-plane and out-of-plane orientation of the magnetization. The first method determines only the difference between $\Delta\nu_Q^{\mathrm{dis}}$ on the Cu sample holder and $\Delta\nu_Q^{\mathrm{dis}}$ on the Fe crystal, the latter method determines $\Delta\nu_Q^{\mathrm{dis}}$ on the Cu sample holder directly. The fact that a consistent description of the data could be obtained with one value for $\Delta\nu_Q^{\mathrm{dis}}$ shows that there was no residual strain-induced EFG, if the foils were soldered on the Fe crystal.

It should also be noted that the quadrupole splitting in the 90° geometry is relatively insensitive to θ as long as $\theta > 45°$. Thus, even if the error in the determination of θ had been underestimated, this would not much affect the final results.

In view of the distinct modification of the electric hyperfine interaction, the question arises whether the magnetic hyperfine splitting is also modified by the lattice distortion of the foils on the Cu sample holder. The respective breaking of the cubic lattice symmetry may indeed cause additional spin-dipole or orbital contributions to the hyperfine field that are of the same order of magnitude as the intrinsic anisotropy of the hyperfine field. However, these contributions do not vary with the direction of the magnetization within the sample plane. Therefore, they do not affect the determination of the intrinsic anisotropy.

B. ^{191}PtFe

The experiments on ^{191}Pt, ^{198}Au, and ^{199}Au were performed before the ^{192}IrFe experiment. Therefore, the effect of the Cu sample holder was not known, the foils were directly soldered to the sample holder, and measurements were performed only in [100] and [110] geometries. Nevertheless, since the in-plane anisotropy of the magnetic hyperfine splitting is not affected by the lattice distortion, and since the intrinsic quadrupole splittings were known from experiments on single-crystal samples, $\nu_m^{[100]} - \nu_m^{[110]}$ and $\Delta\nu_Q^{\mathrm{dis}}$ could be deduced.

Figure 9 shows the ^{191}Pt NMR-ON spectra in [100] and [110] geometries. They could be well described by the superposition of a broad and a narrow resonance. The resonances were interpreted as the ν_1 resonance, which is additionally broadened by the inhomogeneous broadening of the quadrupole splitting, and the ν_2 resonance, which is broadened only by the inhomogeneous broadening of the magnetic hyperfine splitting, since $\nu_2 = \nu_m$ for $I(^{191}\mathrm{Pt}) = 3/2$.

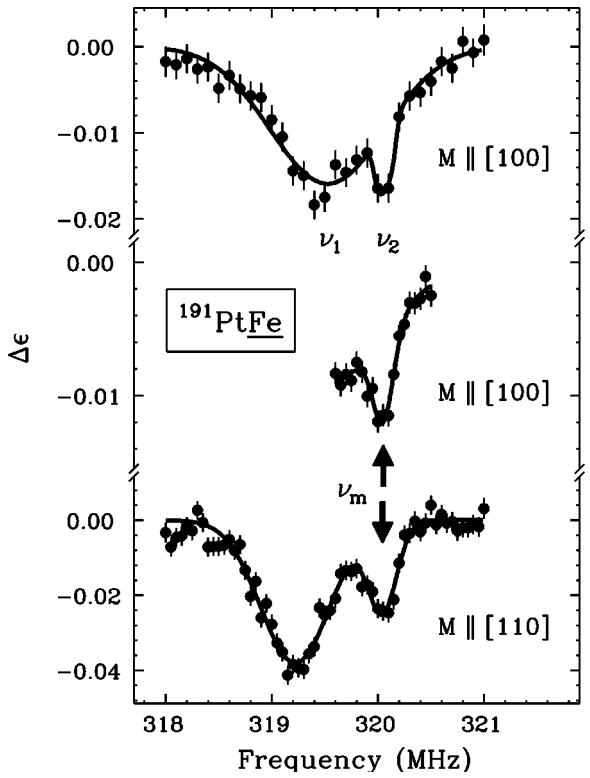

FIG. 9. ^{191}PtFe: NMR-ON spectra in the [100] and [110] geometries at $B_{\mathrm{ext}} = 0.1$ T. $\Delta_{\mathrm{FM}} = \pm 0.1$ MHz (top and bottom) or ± 0.075 MHz (middle). $T = 18$ mK (top), 24 mK (middle), and 15 mK (bottom).

The two resonances were best separated in the [110] geometry. The intensity ratio between the ν_2 and ν_1 resonances, $I_2/I_1 = 0.26(3)$, was in perfect agreement with the expected ratio. For the ν_3 resonance, $I_3/I_1 \approx -0.05$ was expected, which explains the absence of a significant signal from this subresonance. The *least squares* fit analysis of the NMR-ON spectrum yielded: $\nu_m = 320.044(12)$ MHz, $\Delta\nu_Q = +0.822(14)$ MHz, $\Gamma_m = 0.28(3)$ MHz, and $\Gamma_Q = 0.70(4)$ MHz. Γ_m and Γ_Q are the inhomogeneous broadenings of ν_m and $\Delta\nu_Q$, respectively.

In the [100] geometry the ν_2 resonance was less clearly separated, since the quadrupole splitting was broadened by more than 200% and the ν_1 resonance extended beyond the ν_2 resonance. To improve the precision of the determination of ν_m, a small part of the spectrum around the ν_2 resonance was measured again with improved statistics and frequency resolution. The middle part of Fig. 9 shows this spectrum. The *least squares* fit analysis of both spectra yielded $\nu_m = 320.052(10)$ MHz, $\Delta\nu_Q = +0.54(5)$ MHz, $\Gamma_m = 0.20(3)$ MHz, and $\Gamma_Q = 1.26(7)$ MHz.

In the [110] geometry this interpretation of the resonance structure was confirmed by a MAPON measurement. The MAPON spectrum is shown in Fig. 10. Its analysis yielded $\Delta\nu_Q = +0.818(24)$ MHz and $\Gamma_Q = 0.91(8)$ MHz, which is in reasonable agreement with the NMR-ON results.

The intrinsic quadrupole splittings are known from an experiment on a single-crystal sample: $\Delta\nu_Q^{[100]} = +0.13(5)$ MHz and $\Delta\nu_Q^{[110]} = +0.300(11)$ MHz.[12]

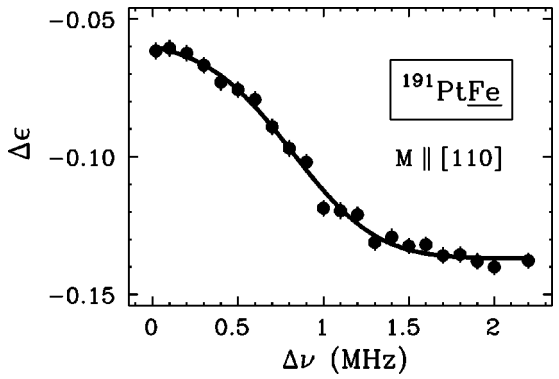

FIG. 10. ^{191}PtFe: MAPON spectrum in the [110] geometry at $B_{ext}=0.1$ T. MAPON sweep from 316.8 to 323.4 MHz in 0.2 s.

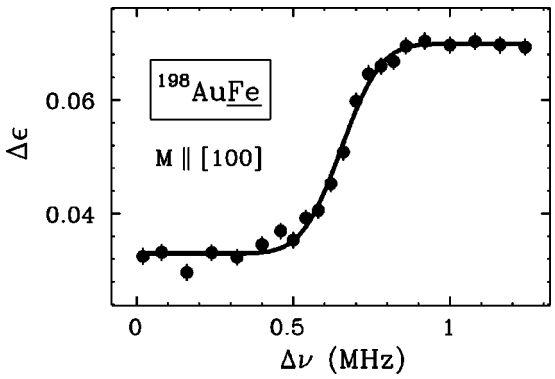

FIG. 12. ^{198}AuFe: MAPON spectrum in [100] geometry at $B_{ext}=0.1$ T. MAPON sweep from 256.9 to 261.9 MHz in 0.2 s.

The difference to the quadrupole splittings in the single-crystalline foils corresponds to

$$\Delta\nu_Q^{dis}=-1.04(6)\ \text{MHz}.$$

The anisotropy of the magnetic hyperfine splitting is

$$\nu_m^{[100]}-\nu_m^{[110]}=+0.01(2)\ \ \text{MHz}.$$

C. ^{198,199}AuFe

For ^{199}Au ($I=3/2$) the subresonance structure was clearly resolved. Figure 11 shows the NMR-ON spectra of ^{199}Au in [100] and [110] geometries.

The *least squares* fit analysis of the NMR-ON spectra yielded the following hyperfine splitting frequencies at $B_{ext}=0.1$ T: $\nu_m=166.536(14)$ MHz and $\Delta\nu_Q=-1.052(14)$ MHz in the [100] geometry, $\nu_m=166.503(11)$ MHz and $\Delta\nu_Q=-0.772(11)$ MHz in the [110] geometry. For convenience we also give the quadrupole splittings in terms of $\Delta\nu_Q$ of ^{198}Au, the more often used isotope for hyperfine interaction studies on Au: According to $\Delta\nu_Q(^{198}\text{Au})/\Delta\nu_Q(^{199}\text{Au})=0.627(5)$,[10] the quoted $\Delta\nu_Q$'s correspond to $\Delta\nu_Q(^{198}\text{Au})=-0.660(10)$ MHz in the [100] geometry and $\Delta\nu_Q(^{198}\text{Au})=-0.484(8)$ MHz in the [110] geometry.

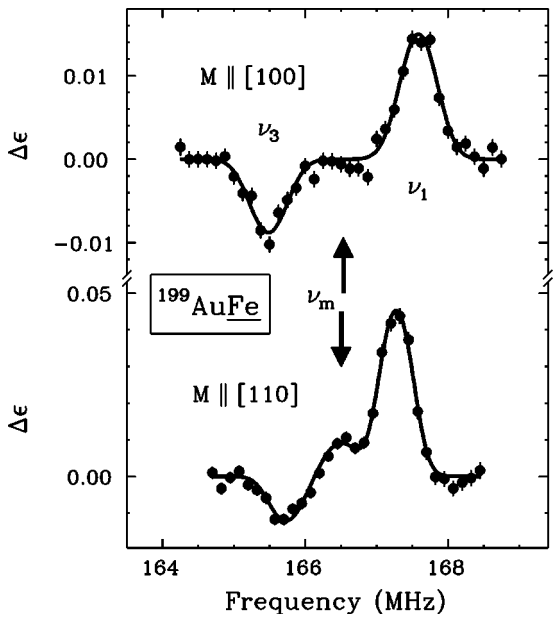

FIG. 11. ^{199}AuFe: NMR-ON spectra in [100] and [110] geometries at $B_{ext}=0.1$ T. $\Delta_{FM}=\pm0.25$ MHz. $T=35(2)$ mK in the [100] geometry and 17(1) mK in the [110] geometry.

In the [100] geometry these results were confirmed by a MAPON measurement on ^{198}Au. The MAPON spectrum is shown in Fig. 12. Its analysis yielded $\Delta\nu_Q(^{198}\text{Au})=-0.653(6)$ MHz, in good agreement with the NMR-ON result.

The intrinsic quadrupole splittings are known from a previous ^{198}AuFe experiment on a single-crystal sample: $\Delta\nu_Q^{[100]}=-0.608(18)$ MHz, $\Delta\nu_Q^{[110]}=-0.399(10)$ MHz.[13] If these data are compared with the quadrupole splittings in the single-crystalline foils,

$$\Delta\nu_Q^{dis}(^{198}\text{Au})=+0.144(30)\ \text{MHz}$$

is obtained. The anisotropy of the magnetic hyperfine splitting is

$$(\nu_m^{[100]}-\nu_m^{[110]})(^{199}\text{Au})=+0.03(2)\ \ \text{MHz}.$$

V. DISCUSSION

A. Strain-induced EFG

Using $Q(^{198}\text{Au})=+0.640(19)$ b,[10] $Q(^{191}\text{Pt})=-0.87(4)$ b,[14] and $V_{zz}^{[100]}(\text{IrFe})=-4.02(5)\times10^{16}$ V/cm^2,[4] the following principal components of the strain-induced EFG are obtained:

$$\text{AuFe: } V_{zz}^{dis}=+0.37(8)\times10^{16}\ \text{V/cm}^2,$$

$$\text{PtFe: } V_{zz}^{dis}=+0.99(7)\times10^{16}\ \text{V/cm}^2,$$

$$\text{IrFe: } V_{zz}^{dis}=+1.36(7)\times10^{16}\ \text{V/cm}^2.$$

These are small EFGs. They correspond to changes in the population numbers of the $5d$ orbitals of the order of 10^{-3}.[4] The following findings supported the hypothesis that the compression of the Fe foils due to the different thermal contraction of the sample holder caused an additional strain-induced EFG.

(i) The deviation of the quadrupole splitting in single-crystalline foils from the quadrupole splitting in single crystals is about the same in [100] and [110] geometries but changes the sign if the sample is magnetized perpendicular to the foil plane. This points to an additional EFG in the single-crystalline foils with symmetry axis perpendicular to the foil plane.

(ii) A thick Fe crystal between the foils and the sample holder completely removes the additional EFG. This shows that the origin of the effect lies outside of the foils.

(iii) An order of magnitude estimate is possible within the point charge model: The relative length changes between room temperature and 5 K are $\delta l/l = -2.04\times10^{-3}$ for Fe and $\delta l/l = -3.24\times10^{-3}$ for Cu.[15] If the Fe foils undergo the same length change as the Cu sample holder, an in-plane strain of $\delta l/l = -1.2\times10^{-3}$ is the result. According to the Poisson ratio of Fe, $\nu = 0.37$, this should be accompanied by a tensile strain perpendicular to the sample plane of $\delta l/l = +1.4\times10^{-3}$.[16] Within the point charge model this tetragonal distortion of the bcc lattice leads to an EFG of about $-2.5\times10^{-3}\,(1-\gamma_\infty)Ze/a^3$.[17] Taking $(1-\gamma_\infty)=50$ for the Sternheimer antishielding factor,[18] $Z=4$ for the effective charge, $a=2.86$ Å for the lattice constant, and taking into account that the EFGs in noncubic group VII*b* and VIII*b* elements are by about a factor of -2 larger than the estimates within the point charge model,[19] we predict $V_{zz}^{\rm dis} = +0.6\times10^{16}$ V/cm^2. This is consistent with the observed order of magnitude and the sign of $V_{zz}^{\rm dis}$. In passing we note that magnetostrictive strains are only of the order of 10^{-5} to 10^{-4}. They are, therefore, negligible in the present context.

The thickness of the sample certainly favors the relaxation of the induced lattice distortion. However, we have no quantitative explanation why the distortion is almost completely relaxed in the bulk single crystals but not in the single-crystalline foils. Accordingly, we also do not know the actual distortion of the lattice in the single-crystalline foils. It may well be smaller than calculated on the basis of the thermal constrictions of Fe and Cu, and it may be sensitive to details of the sample preparation and the soldering procedure. Therefore, the quoted $V_{zz}^{\rm dis}$ should not be regarded as an intrinsic property of the respective impurity host system.

B. Anisotropy of the hyperfine field

The following anisotropies of the hyperfine field can be deduced from the observed magnetic hyperfine splitting frequencies:

$$\text{AuFe:}\quad B_{\rm HF}^{[100]} - B_{\rm HF}^{[110]} = -0.016(9)\ \text{T},$$

$$\text{PtFe:}\quad B_{\rm HF}^{[100]} - B_{\rm HF}^{[110]} = -0.003(6)\ \text{T},$$

$$\text{IrFe:}\quad B_{\rm HF}^{[100]} - B_{\rm HF}^{[110]} = -0.073(8)\ \text{T}.$$

Compared with the total hyperfine field, the anisotropies are only $5.4(6)\times10^{-4}$ for IrFe, $0.2(5)\times10^{-4}$ for PtFe, and $2.0(11)\times10^{-4}$ for AuFe.

The anisotropy of the hyperfine field is a spin-orbit effect. The two main contributions are the anisotropy of the orbital hyperfine field and the anisotropy of the spin-dipole field. The effect provides additional information on the modification of the electronic structure by the spin-orbit coupling. The 5*d* impurities in Fe, which have also been studied via the local orbital moment and the spin-orbit EFG,[4,20] become an experimentally particularly well-studied set of systems in this respect.

The contribution of the local orbital moment to the hyperfine field of the 5*d* impurities in Fe is of the order of 10 T.[21,22] However, in a perturbative treatment of the spin-orbit coupling, in cubic lattice symmetry the orbital moment is isotropic in first order. The dependence on the direction of the magnetization arises only in third order.[5] This introduces an additional factor $(\xi/W)^2$, where the spin-orbit coupling strength ξ is of the order of 0.4 eV for the 5*d* elements and the bandwidth W is of the order of 5 eV.

For a realistic estimate of the orders of magnitude, model calculations were performed using the expressions given in the Appendix. The partial densities of states of the 5*d* impurities in Fe were taken from Ref. 11, where they had been obtained by the full-potential linearized augmented plane-wave method using a supercell with one impurity and seven Fe atoms. ξ and $\langle r^{-3}\rangle$ were taken from Ref. 23, where they had been calculated for the free atom.

According to these calculations, the following orders of magnitude are to be expected: The third-order contribution to the orbital moment is of the order of several percent of the first-order contribution. Its anisotropy is of the order of 10%, leading to a relative anisotropy of the orbital moment of the order of several 10^{-3}. The respective anisotropy of the orbital hyperfine field is of the order of 0.1 T. It is thus a potential source of the observed anisotropy of the hyperfine field.

Although the anisotropy of the orbital moment is very small in cubic lattice symmetry, its study is of general interest, since it is thought to be the main source of the magnetic anisotropy energy and the magnetostriction.[5,24]

The second potential source of the anisotropy of the hyperfine field is the spin-dipole field $B_{\rm dip}$, which arises from the noncubic spin distribution around the nucleus. It is closely related to $V_{z'z'}$, which arises from the noncubic charge distribution. If the contributions of the spin-up ($\uparrow$) electrons and the spin-down ($\downarrow$) electrons are distinguished, this relation can be expressed in the following ways:

$$B_{\rm dip}^{\uparrow} = -0.0644 V_{z'z'}^{\uparrow},$$

$$B_{\rm dip}^{\downarrow} = +0.0644 V_{z'z'}^{\downarrow}, \qquad (9)$$

where $V_{z'z'}$ is expressed in 10^{16} V/cm^2 and $B_{\rm dip}$ in T.

In cubic lattice symmetry both the noncubic spin and the noncubic charge distributions are spin-orbit effects. They arise in second-order perturbation theory and depend already in this order strongly on the direction of the magnetization. The latter feature explains why $B_{\rm dip}$ is important for the anisotropy of $B_{\rm HF}$, but negligible for the much larger isotropic part of $B_{\rm HF}$.

The order of magnitude of the anisotropy of $B_{\rm dip}$ can be estimated via Eq. (9): For the 5*d* impurities in Fe the anisotropy of $V_{z'z'}^{\rm so}$ is in the range 0.1–1.5×10^{16} V/cm^2. Accord-

ingly, the anisotropy of B_{dip} is expected to be in the range 0.005–0.1 T. This also agrees with the magnitude of the observed anisotropies.

Information on B_{dip} provides a more detailed picture of the noncubic charge distribution, since it allows the division into a spin-up and a spin-down part via Eq. (9). Unfortunately, only the anisotropic part of B_{dip} is accessible to the experiment, and only the combined anisotropy of the spin-dipole field and the orbital field is actually measured.

C. Single-crystalline foils for hyperfine interaction studies

The use of single-crystalline foils will enable the study of spin-orbit EFGs and their anisotropy, defect-associated EFGs, nuclear quadrupole moments, and the anisotropy of the hyperfine field in cases where the impurity element is best introduced by alloying or by recoil implantation.

The determination of the quadrupole moment of ^{192}Ir, an isotope which is easily produced by neutron activation, provides an example for this kind of application. Taking $\Delta\nu_Q^{[100]}(^{192}\mathrm{Ir}) = -0.987(14)$ MHz from this work, $I(^{192}\mathrm{Ir}) = 4$, $\Delta\nu_Q^{[100]}(^{188}\mathrm{Ir}) = -6.93(6)$ MHz,[25] $Q(^{188}\mathrm{Ir}) = +0.484(6)$ b,[26] and $I(^{188}\mathrm{Ir}) = 1$, we derive $Q(^{192}\mathrm{Ir}) = +1.93(4)$ b, which is slightly smaller than previously assumed.[26]

In order to measure only the intrinsic hyperfine splitting and to obtain results that are comparable to the results of other experiments, attention must be paid that the thermal constriction of the sample holder does not introduce an additional strain-induced EFG. We have demonstrated that this kind of strain can be avoided, for example, by a thick Fe backing of the foils.

The slight scatter in the orientation of the crystallographic axes will lead to deviations from the nominal crystallographic orientation of the magnetization. However, the resulting error in the hyperfine splitting frequencies is small. For example, if we assume $\Delta\beta = 7°$ and a misorientation of the foils relative to the magnetic field of less than 3°, the mean square angular deviation from the nominal orientation of the magnetization is less than 5°. If the anisotropy of the respective hyperfine splitting is of the form of Eq. (5), this corresponds to an error of less than 3% of the anisotropy.

The strain-induced EFG does not need to be only a disturbance for the determination of the intrinsic EFG. It represents also a possibility of tuning the EFG, which might be useful for the determination of quadrupole moments by NMR-ON and MAPON in special cases. For example, in our experiments the EFG of PtFe was increased by more than 100% by the strain-induced EFG. It should be possible to vary the magnitude of the additional EFG via the substrate of the foils. The technique may also be used to introduce a small EFG with well-defined symmetry axis into nonmagnetic cubic host foils.

Quadrupole splittings from previous NMR-ON experiments on conventional polycrystalline foils are difficult to interpret, since usually neither the texture nor the strain of the samples were investigated.

For example, in the past controversial results were obtained for the quadrupole splitting of ^{191}PtFe (Refs. 27 and 28): In several NMR-ON experiments a more or less distinct two-peak structure of the resonance spectrum was observed. This was interpreted either as a quadrupole splitting, or, since the structure could be made to disappear by annealing of the sample, as a defect-associated structure of the magnetic hyperfine splitting. Our experiments suggest that the resonance structure was indeed of quadrupolar origin, and that the disappearence of the structure was due to a change in the strain-induced EFG.

ACKNOWLEDGMENTS

We wish to thank E. Smolic for experimental help and P. Maier-Komor for the rolling of the Fe foils. The support of the Forschungszentrum Jülich, Zentralabt. Forschungsreaktoren, and of J. Völkl, W. Clauß, G. Neff, M. Stanger, and H. Utz from the Kristall-Labor in the investigation of the texture of the foils is gratefully acknowledged.

APPENDIX: ANISOTROPY OF THE ORBITAL HYPERFINE FIELD IN THIRD-ORDER PERTURBATION THEORY

In Ref. 11 a simple Green's function formalism for spin-orbit effects at heavy impurities in ferromagnetic metals has been derived. The formalism combines the treatment of the spin-orbit coupling in perturbation theory with the tight-binding model and the neglect of the spin-orbit coupling in the host. It allows one to express spin-orbit effects in terms of the spin-orbit coupling strength and the local density of states of the system without spin-orbit coupling. The approach cannot replace *ab initio* calculations, but it reproduces the basic properties of the effect and gives some insight into the underlying physics.

In Ref. 11 the formalism has been applied to the orbital moment and the spin-orbit EFG. Here we give the expression for the orbital moment in third-order perturbation theory. This is the first anisotropic contribution to the orbital moment, since the first-order contribution is isotropic in cubic lattice symmetry, and all even-order contributions vanish.[5,11]

Using the notation of Ref. 11, the third-order contribution to the orbital moment can be expressed in the following form:

$$\langle l_{z'}\rangle^{(3)} = \xi^3 \int^{e_F} \sum_{stuv} \sum_{ijkl} c_{ijkl}^{stuv}\,\Omega_{ijkl}^{stuv}(e)\,de, \tag{A1}$$

$$\Omega_{ijkl}^{stuv}(e) = -(1/\pi)\,\mathrm{Im}[G_i^s(e)G_j^t(e)G_k^u(e)G_l^v(e)], \tag{A2}$$

$$G_i^s(e) = \mathcal{P}\left[\int \frac{\rho_i^s(e')}{(e-e')}\,de'\right] - i\pi\rho_i^s(e), \tag{A3}$$

The superscripts s, t, u, and v denote the spin direction ($\uparrow$ and $\downarrow$ for spin-up and spin-down), the subscripts i, j, k, and l denote the orbital character (t and e for t_{2g} and e_g orbitals) of the involved electron orbitals. The input of Eq. (A1) are the spin-orbit coupling strength ξ and the local partial densities of states $\rho_i^s(e)$ at the impurity.

$\int^{e_F}\Omega_{ijkl}^{stuv}(e')de'$ is the contribution from the admixture of $^{s}_{i}$, $^{t}_{j}$, $^{u}_{k}$, and $^{v}_{l}$ orbitals by the spin-orbit coupling. The individual contributions are weighted by the c_{ijkl}^{stuv} coefficients. The 16 different nonvanishing coefficients are given by

$$
\begin{aligned}
c_{tete}^{\uparrow\uparrow\uparrow\uparrow} &= 4-2F(\boldsymbol{\alpha}),\\
c_{ttte}^{\uparrow\uparrow\uparrow\uparrow} &= 2F(\boldsymbol{\alpha}),\\
c_{tttt}^{\uparrow\uparrow\uparrow\uparrow} &= 1/4,\\
c_{tete}^{\uparrow\uparrow\downarrow\uparrow} &= 2+2F(\boldsymbol{\alpha}),\\
c_{etet}^{\uparrow\uparrow\downarrow\uparrow} &= 2F(\boldsymbol{\alpha}),\\
c_{ttet}^{\uparrow\uparrow\downarrow\uparrow} &= 2-F(\boldsymbol{\alpha}),\\
c_{ttte}^{\uparrow\uparrow\downarrow\uparrow} &= 2-3F(\boldsymbol{\alpha}),\\
c_{tttt}^{\uparrow\uparrow\downarrow\uparrow} &= 1/2,\\
c_{ijkl}^{\downarrow\downarrow\downarrow\downarrow} &= -c_{ijkl}^{\uparrow\uparrow\uparrow\uparrow},\\
c_{ijkl}^{\downarrow\downarrow\uparrow\downarrow} &= -c_{ijkl}^{\uparrow\uparrow\downarrow\uparrow},
\end{aligned}
\tag{A4}
$$

$$
F(\boldsymbol{\alpha}) = 3(\alpha_x^2\alpha_y^2+\alpha_y^2\alpha_z^2+\alpha_z^2\alpha_x^2). \tag{A5}
$$

The dependence of the c_{ijkl}^{stuv}'s on the direction of the magnetization determines the anisotropy. α_x, α_y, and α_z are the directional cosines of the magnetization with respect to the cubic axes. $F(\boldsymbol{\alpha})=0$ for $M\|[100]$, $=3/4$ for $M\|[110]$, and $=1$ for $M\|[111]$.

Equation (A1) was applied to various realistic densities of states. The following general observations were made:

(i) The third-order contribution to the orbital moment is smaller than the first-order contribution by a factor of the order of $10(\xi/W)^2$.

(ii) The anisotropy of the third-order contribution is of the order of 10% or less. One main reason for the small anisotropy can be understood from the c_{ijkl}^{stuv} coefficients of Eq. (A4). For the $\uparrow\uparrow\uparrow\uparrow$ and the $\downarrow\downarrow\downarrow\downarrow$ contributions the e_g orbitals have somewhat more weight for $M\|[100]$ and the t_{2g} orbitals for $M\|[111]$. Just the reverse is true for the $\uparrow\uparrow\downarrow\uparrow$ and the $\downarrow\downarrow\uparrow\downarrow$ contributions. Due to these opposite trends, the anisotropies of the individual contributions largely cancel each other.

(iii) The sensitivity of $\langle l_{z'}\rangle^{(3)}$ to band structure details is comparable to that of the spin-orbit EFG.[11] However, due to the mentioned large cancellation between the individual contributions, the anisotropy of $\langle l_{z'}\rangle^{(3)}$ is distinctly more sensitive. For example, in the $5d$ series from ReFe to AuFe, $\langle l_{z'}\rangle^{[100]}-\langle l_{z'}\rangle^{[111]}$ changes the sign four times, whereas $\langle l_{z'}\rangle^{(3)}$ changes the sign only two times.

Within the tight-binding approach the orbital hyperfine field can be derived from the orbital moment by the following expression:

$$
B_{\mathrm{HF}}^{\mathrm{orb}} = 12.52\langle r^{-3}\rangle\langle l_{z'}\rangle, \tag{A6}
$$

where $\langle r^{-3}\rangle$ is expressed in units of the Bohr radius and $B_{\mathrm{HF}}^{\mathrm{orb}}$ in T.

[1] E. Matthias and R.J. Holliday, Phys. Rev. Lett. **17**, 897 (1966).

[2] P. Herzog, in *Low-Temperature Nuclear Orientation*, edited by N. J. Stone and H. Postma (North-Holland, Amsterdam, 1986), p. 953.

[3] A. Goyal, D.P. Norton, J.D. Budai, M. Paranthaman, E.D. Specht, D.M. Kroeger, D.K. Christen, Q. He, B. Saffian, F.A. List, D.F. Lee, P.M. Martin, C.E. Klabunde, E. Hartfield, and V.K. Sikka, Appl. Phys. Lett. **69**, 1795 (1996).

[4] G. Seewald, E. Zech, E. Hagn, R. Kleyna, M. Voß, A. Burchard, and ISOLDE Collaboration, Phys. Rev. B **66**, 174401 (2002).

[5] P. Bruno, Phys. Rev. B **39**, 865 (1989); in *Ferienkurse des Forschungszentrums Jülich*, edited by R. Hölze (Forschungszentrum Jülich, 1993), Chap. 24.

[6] P. Escudier, Ann. Phys. (Paris) **9**, 125 (1975).

[7] B. D. Cullity, *Elements of X-Ray Diffraction* (Addison-Wesley, Reading, MA, 1978), Chap. 9.

[8] P.T. Callaghan, P.J. Back, and D.H. Chaplin, Phys. Rev. B **37**, 4900 (1988).

[9] P.J. Back, D.H. Chaplin, and P.T. Callaghan, Phys. Rev. B **37**, 4911 (1988).

[10] G. Seewald, E. Hagn, E. Zech, and D. Forkel-Wirth, Nucl. Phys. A **602**, 41 (1996).

[11] G. Seewald, E. Zech, and H. Haas, Phys. Rev. B **66**, 174402 (2002).

[12] G. Seewald, E. Hagn, E. Zech, R. Kleyna, M. Voß, D. Forkel-Wirth, A. Burchard, and ISOLDE Collaboration, Phys. Rev. Lett. **82**, 1024 (1999).

[13] G. Seewald, Ph.D. thesis, TU München, 1999.

[14] Th. Hilberath, St. Becker, G. Bollen, H.-J. Kluge, U. Krönert, G. Passler, J. Rikovska, R. Wyss, and ISOLDE Collaboration, Z. Phys. A **342**, 1 (1992).

[15] Y.S. Touloukian, R.K. Kirby, R.E. Taylor, and P.D. Desai, *Thermal Expansion of Metallic Elements and Alloys* (Plenum, New York, 1975).

[16] D. Sander, Rep. Prog. Phys. **62**, 809 (1999).

[17] F.W. de Wette, Phys. Rev. **123**, 103 (1961).

[18] F.D. Feiock and W.R. Johnson, Phys. Rev. **187**, 39 (1969).

[19] H. Ernst, E. Hagn, E. Zech, and G. Eska, Phys. Rev. B **19**, 4460 (1979).

[20] G. Schütz, M. Knülle, and H. Ebert, Phys. Scr. **T49**, 302 (1993); G. Schütz and P. Fischer, in *Ferienkurse des Forschungszentrum Jülich*, edited by R. Hölze (Forschungszentrum Jülich, 1993), Chap. 22.

[21] P.C. Riedi and E. Hagn, Phys. Rev. B **30**, 5680 (1984).

[22] H. Ebert, R. Zeller, B. Drittler, and P.H. Dederichs, J. Appl. Phys. **67**, 4576 (1990).

[23] S. Fraga, J. Karwowski, and K.M.S. Saxena, *Handbook of Atomic*

Data (Elsevier, Amsterdam, 1976).
[24] O. Hjortstam, K. Baberschke, J.M. Wills, B. Johansson, and O. Eriksson, Phys. Rev. B **55**, 15 026 (1997).
[25] G. Seewald, E. Hagn, E. Zech, D. Forkel-Wirth, A. Burchard, and ISOLDE Collaboration, Phys. Rev. Lett. **78**, 1795 (1997).
[26] G. Seewald, E. Hagn, B. Hinfurtner, E. Zech, D. Forkel-Wirth, R. Eder, and ISOLDE Collaboration, Phys. Rev. Lett. **77**, 5016 (1996).
[27] R. Eder, E. Hagn, and E. Zech, Phys. Lett. B **158**, 371 (1985).
[28] K. Nishimura, S. Ohya, and N. Mutsuro, Hyperfine Interact. **36**, 235 (1987).